

Modeling and assessing the effects of the sea surface, from being flat to being rough and dynamic

Blacqui re, Gerrit; Sertlek, H seyin  zkan

DOI

[10.1190/geo2018-0294.1](https://doi.org/10.1190/geo2018-0294.1)

Publication date

2019

Document Version

Accepted author manuscript

Published in

Geophysics

Citation (APA)

Blacqui re, G., & Sertlek, H.  . (2019). Modeling and assessing the effects of the sea surface, from being flat to being rough and dynamic. *Geophysics*, *84*(2), T13-T27. <https://doi.org/10.1190/geo2018-0294.1>

Important note

To cite this publication, please use the final published version (if applicable).
Please check the document version above.

Copyright

Other than for strictly personal use, it is not permitted to download, forward or distribute the text or part of it, without the consent of the author(s) and/or copyright holder(s), unless the work is under an open content license such as Creative Commons.

Takedown policy

Please contact us and provide details if you believe this document breaches copyrights.
We will remove access to the work immediately and investigate your claim.

Modeling and assessing the effects of the sea surface, from being flat to being rough and dynamic

Gerrit Blacquière* and Hüseyin Özkan Sertlek*

**Delft University of Technology,*

Delft, The Netherlands

email: G.Blacquiere@tudelft.nl; H.O.Sertlek@tudelft.nl

(October 25, 2018)

GEO-2018-0294.R2

Running head: **Modeling the effects of the sea surface**

ABSTRACT

The sea surface acts as a very strong reflector because of the large impedance contrast between water and air. The reflection coefficient is -1 in a very good approximation. Apart from the surface multiples, the sea surface is also responsible for generating the source and receiver ghost wavefields. These cause the well-known ghost notches in the spectrum: areas where the signal-to-noise ratio is very low. To model the ghost wavefields, ghost operators can be computed and applied to ghost-free data. Modeling experiments show that in the case of a flat sea surface, the character of the notches in various gather types, e.g., receiver gather, common-offset gather, shot record, is largely determined by the complexity of the earth. In a simple earth, e.g., horizontally layered, the notches are always well defined and deep, but in a complex earth they become blurry in some of the gather types. Therefore, in the case of a complex subsurface, source deghosting is best carried out in the common receiver domain, and receiver deghosting is best carried out in the common shot domain. In

the case of a simple subsurface, deghosting can be carried out in all domains. An additional factor is that the sea surface may be rough and dynamic. This causes blurry ghost notches in all gather types, even in the case of a simple earth. To model the source ghost for this situation, an effective static rough sea surface suffices. This keeps the computations simple. The condition is that the source has an impulsive character. However, to model the receiver ghost (and the source ghost for a non-impulsive source), the dynamics of the sea surface must be included. This can be done by composing the final result from the results computed for a number of 'frozen' snapshots of the dynamic sea surface.

INTRODUCTION

Because of the huge impedance contrast between water and air, the sea surface acts as an extremely strong reflector. The reflection coefficient is -1 in a very good approximation. The sea-surface reflectivity causes the source and receiver ghosts with the corresponding angle-dependent notches in the frequency-wavenumber spectrum. There is a wealth of literature discussing the modeling of the ghost and providing methods for deghosting. For example, Laws and Kragh (2002) use a Kirchhoff method for computing the ghost in the case of a rough sea surface and focus on the implications on time-lapse data; Mayhan and Weglein (2013) discuss source and receiver deghosting both inside and away from the notch areas using pressure as well as its vertical gradient (particle velocity); Amundsen and Zhou (2013) pay special attention to the low frequencies; Beasley et al. (2013) and Robertsson et al. (2014) use causality of the upcoming wavefield with respect to the downgoing wavefield in a deghosting method based on wave-equation modeling; Egorov et al. (2018) study the effects of a rough sea surface for frequencies up to several kHz; Konuk and Shragge (2018) developed a mimetic finite-difference scheme using a dynamic mesh to compute the effects of the time-varying sea surface, and Cecconello et al. (2018) derived an integral approach to modeling the time-variant reflection of a rough sea surface and who also provide an extensive literature review. In this paper, we introduce a modeling method where the source and/or the receiver ghost can be added to an existing ghost-free data set. This enables us to study the effects of these ghosts individually or combined. We inspect the ghost notches for a flat sea surface in various domains: common-source, common-receiver, zero-offset (ZO), and common-midpoint (CMP) domain. The appearance is different in each of these domains depending on the complexity of the earth. Based on these observations, it becomes clear why selecting the right domain is important in deghosting.

Then the hypothetical case of modeling the effect of a rough yet static, 'frozen', sea surface is discussed, after which the dynamic, or time-variant, character is introduced. Here, a distinction is made between the source ghost and the receiver ghost. To model the source ghost for an impulsive source, an effective static rough sea surface is introduced. The idea is that the source ghost computed with this particular static sea surface approximately equals the one computed with the actual dynamic sea surface. The benefits of this approach are its simplicity and ease of implementation: unlike formulations that incorporate the dynamics of the sea surface, such as discussed by Orji et al. (2012) and Ceconello et al. (2018), in our approach existing methods that can deal with a static rough sea surface can be used to compute the source ghost for the dynamic case. Furthermore, the method is computationally efficient because it is carried out in the frequency domain. The same benefits, except for the computational efficiency gain, apply when modeling the receiver ghost, or the source ghost for a non-impulsive source: in that case, the dynamic sea-surface result is composed from a number of static sea-surface results.

The modeling method can be used to test deghosting algorithms. A deghosting example is given where the reflectivity of a rough sea surface is replaced by an effective reflectivity in combination with a flat sea surface. The final section of the paper briefly touches upon the effect of the sea surface on the surface-related multiples.

THEORY

We start with the ghost model at the source side. The source depth is z_s , which may be spatially variable, i.e. $z_s = z_s(x, y)$. Because of the strong reflectivity at sea-surface level $z_0(x, y)$, the source wavefield has two components: the first is directly travelling down, the second is going up, getting reflected at the sea surface and then travelling down, see the red

arrow and the green arrow, respectively, in Figure 1a.

Using the matrix notation from Berkhout (1985), which is formulated per single frequency component, source matrix \mathbf{S} can be written as:

$$\mathbf{S}(z_s) = \mathbf{G}(z_s, z_s)\mathbf{S}_0(z_s), \quad (1a)$$

with ghost matrix \mathbf{G} given by:

$$\mathbf{G}(z_s, z_s) = \mathbf{I}(z_s, z_s) + \mathbf{W}^+(z_s, z_0)\mathbf{R}(z_0, z_0)\mathbf{W}^-(z_0, z_s). \quad (1b)$$

In equation 1a each column of source matrix \mathbf{S} describes the location, directivity and strength of one source plus its ghost. For example, the amplitude and phase of one frequency component of the wavefield emitted by an airgun array, including its ghost, would be contained in one column of \mathbf{S} , where the individual elements correspond to the spatial locations x and y . Source matrix \mathbf{S}_0 refers to the ghost-free situation. In equation 1b matrix \mathbf{R} describes the surface reflectivity. Matrix \mathbf{W} describes depth extrapolation and superscripts - and + describe the up- and downward direction respectively. More information on the operators \mathbf{W} is provided by Holberg (1988), Blacquière et al. (1989), and Thorbecke et al. (2004). In the case of no lateral changes, such as in the case of a flat sea surface, the matrix multiplications in equations 1a and 1b can be carried out as scalar multiplications in the frequency-wavenumber domain, where the extrapolation operators are given by $\tilde{\mathbf{W}}^\mp(z_1, z_2) = \exp(\pm jk_z \Delta z)$, with $k_z = \sqrt{k^2 - k_x^2 - k_y^2}$ and $\Delta z = z_2 - z_1$. The tilde symbol refers to the wavenumber domain, $k = 2\pi f/c$ is the angular wavenumber, f the frequency, c the speed of sound and k_x , k_y and k_z are respectively the x , y and z components of wave vector \mathbf{k} .

The model for 3-D seismic data including the source ghost is:

$$\mathbf{P}(z_0; z_s) = \mathbf{D}_0(z_0)\mathbf{X}_0(z_0, z_s)\mathbf{G}(z_s, z_s)\mathbf{S}_0(z_s), \quad (2)$$

where $\mathbf{D}_0(z_0)$ is the receiver matrix, also called detector matrix, for receivers located at level z_0 . Each row describes the location, directivity and sensitivity of one receiver or receiver array. Matrix \mathbf{X}_0 is the earth's transfer function, describing wave propagation in the complex subsurface including internal multiples (the inclusion of surface-related multiples will be discussed later). Each column of data matrix \mathbf{P} is a monochromatic shot record and each row a monochromatic receiver gather. The model can be extended with the receiver ghost as well, see Figure 1b. The expression for data that contains both the source and receiver ghost is:

$$\mathbf{P}(z_d; z_s) = \mathbf{D}_0(z_d)\mathbf{G}(z_d, z_d)\mathbf{X}_0(z_d, z_s)\mathbf{G}(z_s, z_s)\mathbf{S}_0(z_s), \quad (3)$$

where the receivers are located at depth level $z_d = z_d(x, y)$.

Using the fact that the reflectivity may be considered to be -1, the ghost matrix becomes:

$$\mathbf{G}(z, z) = \mathbf{I}(z, z) - \mathbf{W}^+(z, z_0)\mathbf{W}^-(z_0, z), \quad (4)$$

where $z = z_s$ for the source ghost and $z = z_d$ for the receiver ghost.

In this paper, when modeling, we focus on the effect of the ghosts and, therefore, we assume perfect spatial sampling, i.e., the spatial sampling distances of both sources and receivers satisfy the Nyquist criterion. In addition, we assume that the sources and receivers are point sources and point receivers. In our formulation this means that both \mathbf{S}_0 and \mathbf{D}_0 may be replaced by identity matrix \mathbf{I} , ignoring the complex scaling factors representing the source and receiver spectrum values respectively, and equation 3 becomes:

$$\mathbf{P}(z_d; z_s) = \mathbf{G}(z_d, z_d)\mathbf{X}_0(z_d, z_s)\mathbf{G}(z_s, z_s). \quad (5)$$

For the moment, we assume constant source and receiver levels z_s and z_d and a flat sea

surface, i.e., $z_0 = z_c$, where z_c is constant. Later, the case of a rough sea surface will be discussed and, finally, the dynamic character of the sea surface will be addressed.

APPEARANCE OF THE GHOST NOTCHES

To illustrate how the ghost notches appear in several domains (for example, common shot domain, common receiver domain, etc.) for a complex subsurface, the Marmousi model shown in Figure 2 was used to create 2-D finite-difference data. To mimic a marine situation, a water layer with a thickness of 250 m and a velocity of 1500 m/s was put on top of the original model. The spatial sampling of sources and receivers is 7.5 m, the spatial size of the model is 6000 m and the maximum frequency is just below 100 Hz. The sources and receivers are located at $z_s = 30$ m and $z_d = 20$ m respectively. However, the influence of the sea surface is not included in this data: as far as the finite-difference modeling is concerned, there is no water-air interface but just water, i.e., the modeled data is ghost free. Because of the perfect spatial sampling for the used frequency band, earth transfer function $\mathbf{X}_0(z_d, z_s)$ in equation 5 corresponds to one frequency component of the finite-difference data. Note that here \mathbf{X}_0 includes the source spectrum value as was defined in the finite-difference modeling. A typical ghost-free shot record and its frequency-wavenumber (k_x, f) spectrum are shown in Figures 3a and 3b, respectively. Because of reciprocity, a typical receiver gather would look identical.

As a start, only the source ghost was added by applying the ghost operator from equation 4 with $z_s = 30$ m to the finite-difference data: $\mathbf{P}(z_d; z_s) = \mathbf{X}_0(z_d, z_s)\mathbf{G}(z_s)$, see Figures 4a and 4b, where the frequency-wavenumber spectra of a shot record and a receiver gather are shown, respectively. The source-ghost notches are clearly seen in the receiver gather, related to a row of $\mathbf{P}(z_d; z_s)$. The horizontal wavenumber in a receiver gather is related to

emission angle α_s , see Figure 1a, because the spatial Fourier transform is over the source coordinate. It is given by $\alpha_s = \arcsin [ck_{x,s}/(2\pi f)]$, where $k_{x,s}$ is the horizontal wavenumber of a receiver gather in the frequency-wavenumber domain. As expected, for $k_{x,s} = 0 \text{ m}^{-1}$ the notches can be found at multiples of 25 Hz. One of the most important notches is the one at 0 Hz: it attenuates the very low frequencies, which are indispensable in FWI (full waveform inversion) and impedance estimation.

However, notches are hardly visible in the shot record, related to a column of $\mathbf{P}(z_d; z_s)$: here, only a vague imprint of the notches can be seen (Figure 4a). The explanation is that in the shot-record spectrum the horizontal wavenumber is no longer related to emission angle α_s , but to incidence angle α_d , see Figure 1b, because the spatial Fourier transform is over the receiver coordinate. The expression for the incidence angle is $\alpha_d = \arcsin [ck_{x,d}/(2\pi f)]$, where $k_{x,d}$ is the horizontal wavenumber of a shot record in the frequency-wavenumber domain. If the subsurface is complex, as is the case in the Marmousi model, the relation between the emission and incidence angles is not straightforward: angles may change during propagation. Consequently, energy emitted at a certain angle α_s may arrive at one or more other angles α_d , and this effect is space and time dependent. Similarly, energy may arrive at angles that have never been emitted, and, consequently, source-ghost notches that are deep and clear in a receiver gather may almost be absent in a shot record.

For the receiver ghost, it is the other way around. This is clear from Figure 5, which shows the case of the receiver ghost only, i.e., $\mathbf{P}(z_d; z_s) = \mathbf{G}(z_d)\mathbf{X}_0(z_d, z_s)$, for $z_d = 20$ m. As expected, at zero spatial wavenumber the receiver-ghost notches clearly show up at multiples of 37.5 Hz (including 0 Hz) in the shot record in Figure 5a, where the wavenumber axis is related to the incidence angles, but not so clearly in the receiver gather in Figure 5b.

Finally, Figures 6a and 6b show the case where both the receiver ghost and the source ghost are included: $\mathbf{P}(z_d; z_s) = \mathbf{G}(z_d)\mathbf{X}_0(z_d, z_s)\mathbf{G}(z_s)$. In this figure, the results of the previous cases are combined. The 75 Hz notch is a "double" one as it is both a source- and a receiver-ghost notch.

This example illustrates that by observing shot-record spectra in the case of complex media, the receiver-ghost notches are clearly visible, but the source-ghost notches are not. One may even get the impression the source ghost is absent. To clearly see it, one must look at receiver-gather spectra, where the conclusion may be opposite.

To illustrate that it is indeed the complexity of the subsurface that causes this behaviour in the different domains as discussed, the simple situation of a single horizontal reflector was chosen. In such a medium, the emission angles are the same as the incidence angles, albeit with an opposite sign. Hence, the source- as well as receiver-ghost notches show up in shot records as well as receiver gathers. This property is shown in Figures 7a and 7b.

We now look at the Marmousi data in other domains. The results for the zero-offset domain, related to the diagonal elements of $\mathbf{P}(z_d; z_s)$, are shown in Figure 8. In this figure the $k_x = 0 \text{ m}^{-1}$ component was removed as it would dominate the figure, mainly because of the strong reflection from the horizontal water bottom. Both the source ghost and the receiver ghost are visible. In the zero-offset domain, the lateral direction refers to the source coordinate as well as to the receiver coordinate, since source and receiver coincide. Therefore, the corresponding horizontal wavenumber refers to both emission and incidence angles.

A closer comparison with a receiver gather however reveals that the notches in the zero-offset domain are not so deep as the ones in the common-receiver domain, see Figure 9

for the case of the source ghost only ($z_s = 30$ m). The explanation is that in the case of zero-offset data most reflections are normal incidence reflections, meaning that the angles at which energy is emitted are the same as the angles at which energy is received. However, in complex media there may be situations where non-normal incidence reflections may be present in a zero-offset trace. It means that the emission and incidence angles are different, which fills the notches.

The notches in the common-midpoint (CMP) domain are shown in Figure 10. For this purpose, the antidiagonal elements of $\mathbf{P}(z_d; z_s)$ were selected. Because the offset sampling interval of the CMP gathers is double the spatial sampling interval of 7.5 m, spatial aliasing is introduced for frequencies higher than 50 Hz. In a CMP gather, an emission angle may differ from its corresponding incidence angle. This explains the blurred, asymmetric notches in Figure 10.

These examples illustrate that the appearance of the notches strongly depends on the domain of observation as well as on the complexity of the earth. This insight also confirms the choice of domain best suited for deghosting (Amundsen and Zhou, 2013), i.e., in complex media, the best domain for source deghosting is the common receiver domain (processing of receiver gathers) and the best domain for receiver deghosting is the common source domain (processing of shot records). In the case of simple media, source and receiver deghosting can be carried out in any domain.

In practice, the source sampling is often relatively coarse in comparison with the receiver sampling. In this case, one faces the dilemma in which domain to carry out the source deghosting: the preferred domain for source deghosting, i.e., the common receiver domain, suffers from aliasing, whereas the domain with less aliasing, i.e., the common shot domain, is

not the domain best suited for source deghosting. To give some insight in the consequences related to this dilemma, the following example is provided. Starting with Marmousi data that contains the source ghost for sources located at a depth of $z_s = 30$ m, two source-deghosting results were obtained, one from deghosting carried out in the common shot domain, see Figure 11, and one from deghosting carried out in the common receiver domain, see Figure 12. Both figures show respectively the data with ghost, data without ghost, deghosted data and the error. In both cases the sampling was sufficiently dense to avoid aliasing. Hence, this example illustrates the effect of carrying out deghosting in the 'wrong' domain. To get an optimum result for the common-shot-domain source deghosting, an adaptive method was used, based on the method discussed by Vrolijk and Blacquiere (2017), where local deghosting operators were estimated, i.e., these operators vary with space and time. In this numerical experiment the error could be obtained from the difference between the data without ghost and the deghosted result, i.e., $\mathbf{X}_0 - \langle \mathbf{X}_0 \rangle$, where $\langle \mathbf{X}_0 \rangle$ represents the deghosted data. We call this difference the deghosting noise and computed the signal-to-deghosting-noise ratio (SNR) according to

$$\text{SNR} = 10 \log_{10} \left\{ \sum_{\omega} (|\mathbf{X}_0|_F^2 / |\mathbf{X}_0 - \langle \mathbf{X}_0 \rangle|_F^2) \right\}, \quad (6)$$

where subscript F indicates the Frobenius norm. As expected, deghosting in the 'wrong' domain yields the smallest SNR: in this example it is 9.4 dB for source-deghosting in the common-receiver domain versus 21 dB obtained for source-deghosting in the common-source domain. This is the price to be paid for deghosting in the 'wrong' domain. It should be balanced by the aliasing problem to be solved when deghosting is to be carried out in the 'preferred' domain in case of a coarse source sampling.

SCATTERING FROM A ROUGH SEA SURFACE

Obviously, a rough sea surface has its effect on the ghost response. The shape of such a sea surface can be modeled using the method discussed by Pierson and Moskowitz (1964). It was used to create sea-surface shapes for different sea states. In Figure 13, surfaces obtained in this way are shown for sea states 0 to 9. See Table 1 for a description and the significant wave height (SWH) of the various sea states (Ainslie, 2010).

We now start with the hypothetical case of a static ('frozen') rough sea surface, although it will be argued later that this case is sufficient for describing the source ghost in the case of a dynamic rough sea surface. The downgoing wavefield $P^+(\mathbf{r})$ scattered by a rough sea, where \mathbf{r} is the vector pointing from the source, being located in the origin at $(x, y, z) = (0, 0, z_s)$, to the observation point, can be calculated by the Kirchhoff-Helmholtz integral (Laws and Kragh, 2002; Robertsson et al., 2006). The choice for this method was based on its efficiency. If preferred, one could use alternative methods, such as finite-difference modeling. In the frequency domain the expression of the Kirchhoff-Helmholtz integral is:

$$P^+(\mathbf{r}) = \frac{1}{4\pi} \int_A \left[G(\mathbf{r}_2) \frac{\partial P^-(\mathbf{r}_1)}{\partial n} - P^-(\mathbf{r}_1) \frac{\partial G(\mathbf{r}_2)}{\partial n} \right] dA, \quad (7)$$

where the Green's function of free space is $G(\mathbf{r}_2) = \frac{\exp(-ik|\mathbf{r}_2|)}{4\pi|\mathbf{r}_2|}$, and the upgoing wavefield incident to the sea surface is $P^-(\mathbf{r}_1) = S \frac{\exp(-ik|\mathbf{r}_1|)}{|\mathbf{r}_1|}$, with S representing amplitude and phase (for the current frequency) of the source. In this formulation, the reflection coefficient of the water-air interface was taken to be -1. The vectors \mathbf{r}_1 and \mathbf{r}_2 are, respectively, the vector from the source to the sea surface and the vector from the sea surface to the observation point, see also Figure 14. The integration area of the sea surface is given by A having an average level of z_0 .

The Kirchhoff-Helmholtz integral equation was numerically solved for each elementary

area ΔA of the rough sea surface under consideration. We used elementary areas of 3×3 m². Once carried for all sources, the result corresponds to the information represented by matrix product $\mathbf{W}^+(z_s, z_0)\mathbf{W}^-(z_0, z_s)$ in the source-ghost matrix (see equation 4). The receiver-ghost matrix was computed similarly.

In this way source- and receiver-ghost matrices were obtained for several sea states. Then test data sets were modeled according to equation 5, i.e., the ghost matrices, which were computed for the 2D case, were applied to the ghost-free Marmousi data discussed earlier. In Figure 15, the wavenumber spectra of some shot and receiver gathers obtained in this way are shown for sea states 0, 6 and 9 with $z_s = 30$ m and $z_d = 20$ m.

For computational efficiency, a reduced portion of the seismic data (between 1.5 km to 4.5 km) was used, which explains the minor differences with previous spectra of sea state 0, compare Figures 6 and 15. However, the notch areas are very similar. Figure 15 shows that indeed the notches are affected by the rough sea surface. For sea state 6, the notches are somewhat dispersed, but for sea state 9, all notches are severely blurred.

The rough sea effects can also be seen in the space-time domain. In Figure 16, these effects are shown for a sinusoidal sea surface and for a surface related to sea state 6, both for sources at $z_s = 30$ m. These figures clearly show the space-dependent imprint of the rough sea surface on the ghost response.

DYNAMIC ROUGH SEA SURFACE

To introduce a dynamic rough sea surface in the modeling, first a dynamic sea surface model must be available, describing the shape of the sea surface as a function of time with a realistic wave shape and motion, see for example Laws and Kragh (2002). Next,

a distinction between the source ghost and the receiver ghost is made. We start with the case of an impulsive source, such as an airgun array, because for this situation the dynamic rough sea surface can be approximated by an effective static rough sea surface. This is because the source signal hits the sea surface only once at a particular location (ignoring possible double reflections in the case of a rough sea surface) and at a particular time. It is the shape of the sea surface at that location and at that moment in time that determines the source ghost. This is explained in Figure 17a. From this figure it becomes clear that the effective rough sea surface is composed of the parts corresponding to times T_1, T_2, \dots, T_N , where N is the number of time samples. Although the example is in 2-D, it can be easily extended to 3-D, where surfaces 1 to N have ring-like shapes, see the four time-snapshots in Figure 17b. Consequently, modeling a shot record with a source ghost in the case of a dynamic rough sea surface comes down to modeling the source ghost using an effective static rough sea surface, and the theory as discussed earlier is applicable to this situation. Doppler effects are ignored in this approximation. Note that for each shot record a different effective static sea surface is required because of the different shot position and the different shot activation time. It means that in this case the computations have to be carried out per individual shot record. Consequently, when observed in a receiver gather, the source ghost wavefield will contain trace-to-trace jitter. An example of a receiver gather that contains the source ghost for the case of a dynamic sea surface is given in Figure 18. The mentioned jitter, which is only present in the ghost wavefield, but not in the direct wavefield, is best observed in the inset shown in Figure 18a. Depending on the source type and its deployment, the source depth may not be constant in the case of a rough sea. For example, an airgun array is usually floating, which means that its depth is influenced by the local sea surface, i.e., the shape of the sea surface right above the airgun array (Laws and

Kragh, 2002) at the time of its activation. As a consequence, not only the ghost wavefield is affected but also the direct wavefield (that has not reflected against the sea surface), causing a static-like effect that increases the trace-to-trace jitter mentioned. This effect is included in our formulation as both z_s and z_0 are a function of space in equation 4. Finally, it is remarked that the individual airguns of the array should possibly not be considered as impulsive sources because of the bubble oscillation, which may cause their interaction with the sea surface to last for several seconds. Although the airgun array has been designed to minimize this effect, the dynamic sea surface may cause some distortion here. In that case, one may wish to take into account the dynamics for the duration of this effect, which is discussed in the next section.

For modeling the receiver ghost, a static rough sea surface does not suffice. Each of the upgoing waves interacts with the sea surface to create a receiver-side ghost, and the shape of the sea surface may change significantly during the recording of seismic waves. To include the dynamic property of the sea surface in the modeling of a shot record with our frequency-domain algorithm, we repeated the modeling exercise for all time instances. In each modeling exercise the rough static sea surface corresponded to the particular time instance. Finally, we obtained a single shot record by selecting the correct instances of time from the computed results, see Figure 19. This way of dealing with the dynamics of the sea surface has the benefit that a simple 'static model' can be used, albeit many times, and that an existing algorithm could be used with minor modifications. An example is shown in Figure 20a, where sea surfaces at T_1, T_2, \dots, T_N were used to model N intermediate results from which the final result was composed. In Figure 20b the modeled result for the static rough sea surface at T_1 is shown for comparison. In both cases the significant wave height is 3.5 m. The difference is shown in Figure 20c. Note that initially the two situations are

rather similar, but, as time progresses, the differences increase, as expected. The difference expressed as an SNR defined similarly as in equation 6 amounts 20 dB.

Obviously, the alternative is to use a time-domain method that is capable of dealing with the sea surface dynamics, such as the ones discussed by Ceconello et al. (2018) and Konuk and Shragge (2018). These have the advantage that multiple reflections can be correctly taken into account as well.

APPROACHES FOR DEALING WITH THE DYNAMIC ROUGH SURFACE IN PROCESSING

To deal with the rough, dynamic sea surface in processing, for example in deghosting, two options can be distinguished, an exact one and an approximate one:

- The first, exact option involves obtaining the shape of the rough sea surface, i.e., $z_0 = z_0(x, y, t)$, in one way or the other and using that information in the process. In other words, both the scattered and the reflected parts of the ghost wavefield are taken into account correctly. This method has been discussed a.o. by King and Poole (2015) and Telling and Grion (2017)
- The second option is to approximate the dynamic rough sea surface by a flat sea surface in combination with an effective reflectivity operator that describes the part of the waves that is reflected according to Snell's law. The benefits of this approximation are its computational simplicity and efficiency. In this approximation, the absolute value of the surface reflectivity is less than 1. The scattered part of the wavefield is ignored and hence this part should either be addressed separately, or it will manifest itself as noise.

We now discuss the second option in some more detail. To compute the effective reflectivity operator needed in this option, we adopt the following approach. Assuming a time-invariant, rough sea surface for the moment, we have seen that the exact ghost operator for this case is (equation 4):

$$\mathbf{G}(z, z) = \mathbf{I}(z, z) - \mathbf{W}^+(z, z_0)\mathbf{W}^-(z_0, z), \quad (8)$$

where $z = z_s(x, y)$ for the source ghost operator and $z = z_d(x, y)$ for the receiver ghost operator. The sea surface shape is $z_0 = z_0(x, y)$. It should be representative for the particular sea-state under consideration.

The ghost operator related to the approximate option is (see also equation 1b):

$$\bar{\mathbf{G}}(z, z) = \mathbf{I}(z, z) + \mathbf{W}^+(z, z_c)\bar{\mathbf{R}}(z_c, z_c)\mathbf{W}^-(z_c, z), \quad (9)$$

where constant z_c represents the average sea surface level and matrix $\bar{\mathbf{R}}$ is the effective reflectivity operator we look for. It should be chosen such that the following residue is minimum:

$$\underset{\bar{\mathbf{R}}(z_c, z_c)}{\text{minimize}} \quad \|\bar{\mathbf{G}}(z, z) - \mathbf{G}(z, z)\|. \quad (10)$$

The effective reflectivity $\bar{\mathbf{R}}$ can be parameterized in several ways, for example, it could be taken to be constant, or frequency dependent, or frequency and angle dependent. An example of the latter is shown in Figure 21. It has been obtained by averaging the results of many realizations of a rough sea surface for a certain sea state. This result is in agreement with similar results obtained by Orji et al. (2013) and Kryvohuz and Campman (2016). An example of applying this method to modeled data is shown in Figure 22. The original data with ghost for a significant wave height of 3.5 m is shown in Figure 22a, the result of deghosting with the optimized effective $\bar{\mathbf{R}}(\alpha, f)$ in Figure 22b, and the residue, multiplied

by 10 to improve the visibility, in Figure 22c. This residue can be used to compute an SNR, similar to the one defined in equation 6, as a measure of the quality of the approximation. Its value for the case shown in Figure 22 is 23.7 dB. It turns out that this SNR is not strongly dependent on the parameterization of $\bar{\mathbf{R}}$. For example, we obtained the SNR's as provided in Table 2 for four approximations of the rough sea-surface reflectivity and two values of the SWH being 3.5 m and 10 m, respectively. We go from simply taking $\bar{\mathbf{R}} = -1$, via the optimum constant, being $\bar{\mathbf{R}} = -0.91$ for SWH = 3.5 m and $\bar{\mathbf{R}} = -0.99$ for SWH = 10 m, and via the optimum frequency-dependent result $\bar{\mathbf{R}}(f)$, to the optimum frequency-and-angle-dependent result $\bar{\mathbf{R}}(\alpha, f)$. The obtained SNR's hardly improve for the more advanced parameterizations of $\bar{\mathbf{R}}$, both for the lower and higher value of the SWH. It means that a simple parameterization, such as $\bar{\mathbf{R}}$ is constant, is sufficient. For the extreme case of an SWH of 10 m, the results obtained for the various choices of $\bar{\mathbf{R}}$ are rather disappointing. Obviously, the model now only explains a relatively small part of the wavefield scattered at the sea surface. This result is a plea for the use of a more advanced method to deal with the effects of the rough sea surface.

MULTIPLE REFLECTIONS

Apart from the ghost wavefields, the surface-related multiples also interact with the sea surface. Following Berkhout (1985), the expression for modeling the ghosts for a static sea surface (equation 3), can be easily extended to include the surface-related multiples as well:

$$\mathbf{P}(z_d; z_s) = \mathbf{D}_0(z_d)\mathbf{G}(z_d, z_d)\mathbf{P}_0(z_d, z_s), \quad (11a)$$

with

$$\mathbf{P}_0(z_d, z_s) = \mathbf{X}_0(z_d, z_s)[\mathbf{G}(z_s, z_s)\mathbf{S}_0(z_s) - \mathbf{W}^+(z_s, z_0)\mathbf{W}^-(z_0, z_d)\mathbf{P}_0(z_d, z_s)]. \quad (11b)$$

Equation 11b is an implicit equation as the total upgoing wavefield $\mathbf{P}_0(z_d, z_s)$ appears both at the left and at the right side of the equation. It can be solved in an iterative way. Starting with $\mathbf{P}_0(z_d, z_s)$ being empty, each next iteration could use $\mathbf{P}_0(z_d, z_s)$ from the previous iteration to add one more order of surface-related multiples. In this way, the fact that first-order multiples interact once with the sea surface, second-order multiples twice and so forth is automatically included. As a consequence, the imprint of the sea surface becomes stronger for higher order multiples (although the amplitude of the multiples weakens with each next order). Therefore, it is important to not only study the effects of the sea-surface imprint on the ghost wavefields, but also on the surface-related multiples. This is one of our current research topics.

Multiple reflections have multiple interactions with the sea surface at various instances of time and the correspondent different shapes of the sea surface. This means that for the case of a dynamic sea surface, the method discussed above is no longer valid, and a modeling method capable of dealing with such a surface (Cecconello et al., 2018; Konuk and Shragge, 2018) is required.

CONCLUSIONS

In marine acquisition, the source and receiver ghost cause angle-dependent notches in the frequency-wavenumber spectrum. In the case of a flat sea surface the source and receiver ghost effects can simply be added to modeled ghost-free data by multiplication with the respective ghost operators. In the case of a complex subsurface, receiver-ghost notches are deep and clearly present in shot-record spectra, but source-ghost notches are hardly visible there. Similarly, source-ghost notches are deep and clearly present in receiver-gather spectra, but receiver-ghost notches are hardly visible there. In other domains, like the ZO

and CMP domains, ghost notches lose much of their definition. They become more blurred with increasing complexity of the medium.

In complex media, the best domain for source deghosting is therefore the common receiver domain, i.e., processing of receiver gathers. Likewise, the best domain for receiver deghosting is the common source domain, i.e., processing of shot records. In the case of a simple subsurface, the source and receiver ghosts are deep and clearly present in all domains and therefore source and receiver deghosting can be carried out in any domain.

Apart from the complexity of the earth, also the roughness of the sea surface has a blurring effect on the ghost notches. Unlike the effect of the earth's complexity, this effect is present in all domains. Modeling this effect is useful to study the performance of deghosting algorithms.

To model the effect of a rough and dynamic sea surface on the source ghost, an effective static rough sea surface can be used. This is beneficial for the computational simplicity. Also, it allows for modeling in the frequency domain, which adds to the computational efficiency. The condition is that the source has an impulsive character.

Such an effective static rough sea surface does not suffice when modeling the receiver ghost, or the source ghost in case the source character is not impulsive, for example in the case of a marine vibrator. In such cases the dynamic character of the rough sea surface has to be included. An option to do this is to compose the dynamic result from a number of static results. This has the advantage that the modeling algorithm stays the same. The modeling of the source and receiver ghosts for the case of a rough and dynamic sea surface can be used to study the quality of deghosting algorithms. For example, the approximation regularly used in deghosting, where the rough and dynamic sea surface is replaced by a flat

sea surface in combination with an effective reflectivity, turns out to be rather poor for high sea states, even when that reflectivity is allowed to be frequency and angle dependent.

The same rough and dynamic sea surface that has its imprint on the ghost wavefields also has its imprint on the surface-related multiples. The higher the multiple order, the stronger the imprint of the rough sea surface. It is therefore important to not only study the effects on the ghost wavefields, but also on the multiples.

ACKNOWLEDGMENTS

We acknowledge the sponsors of the Delphi consortium for the stimulating discussions during the Delphi meetings and their financial support. We acknowledge Jan-Willem Vrolijk for generating the Marmousi data.

REFERENCES

- Ainslie, M. A., 2010, Principles of sonar performance modelling: Axel Springer.
- Amundsen, L., and H. Zhou, 2013, Low-frequency seismic deghosting: *Geophysics*, **78**, WA15–WA20.
- Beasley, C. J., R. Coates, Y. Ji, and J. Perdomo, 2013, Wave equation receiver deghosting: a provocative example: *SEG Technical Program Expanded Abstracts*, **32**, 4226–4230.
- Berkhout, A. J., 1985, *Seismic migration, volume a: Theoretical aspects*, 3rd edn.: Elsevier.
- Blacquièrè, G., H. W. J. Debye, C. P. A. Wapenaar, and A. J. Berkhout, 1989, 3-D table-driven migration: *Geophys. Prosp.*, **37**, 925–958.
- Cecconello, E., E. G. Asgedom, O. C. Orji, M. W. Pedersen, and W. Sllner, 2018, Modeling scattering effects from time-varying sea surface based on acoustic reciprocity: *Geophysics*, **83**, T49–T68.
- Egorov, A., S. Glubokovskikh, A. Bna, R. Pevzner, B. Gurevich, and M. Tokarev, 2018, How rough sea affects marine seismic data and deghosting procedures: *Geophys. Prosp.*, **66**, 3–12.
- Holberg, O., 1988, Towards optimum one-way wave propagation: *Geophys. Prosp.*, **36**, 99–114.
- King, S., and G. Poole, 2015, Hydrophone-only receiver deghosting using a variable sea surface datum: *SEG Technical Program Expanded Abstracts 2015*, 4610–4614.
- Konuk, T., and J. Shragge, 2018, Mimetic finite difference modeling of time-varying sea surface effects on seismic data: *SEG Technical Program Expanded Abstracts 2018*, 3948–3952.
- Kryvohuz, M., and X. Campman, 2016, Optimization of sea surface reflection coefficient and source geometry in conventional dual source flip/flop marine seismic acquisition: *SEG*

- Technical Program Expanded Abstract, 188–192.
- Laws, R., and E. Kragh, 2002, Rough seas and time-lapse seismic: *Geophys. Prosp.*, **50**, 195–208.
- Mayhan, J. D., and A. B. Weglein, 2013, First application of green’s theorem-derived source and receiver deghosting on deep-water gulf of mexico synthetic (seam) and field data: *Geophysics*, **78**, WA77–WA89.
- Orji, O. C., W. Sollner, and L.-J. Gelius, 2012, Effects of time-varying sea surface in marine seismic data: *Geophysics*, **77**, P33–P43.
- , 2013, Sea surface reflection coefficient estimation: *SEG Technical Program Expanded Abstracts*, 51–55.
- Pierson, W., and L. Moskowitz, 1964, A proposed spectral form for fully developed wind seas based on the similarity theory of s.a. kitaigorodskii: *J. Geophys. Res.*, **69**, 5181–5190.
- Robertsson, J. O. A., L. Amundsen, and O. Pedersen, 2014, Deghosting of arbitrarily depth-varying marine hydrophone streamer data by time-space domain modelling: *SEG Technical Program Expanded Abstracts*, **33**, 4248–4252.
- Robertsson, J. O. A., R. Laws, C. Chapman, J.-P. Vilotte, and E. Delavaud, 2006, Modelling of scattering of seismic waves from a corrugated rough sea surface: a comparison of three methods: *Geophys. J. Int.*, **167**, 70–76.
- Telling, R., and S. Grion, 2017, Estimation of a time-varying sea-surface profile for receiver-side deghosting: *SEG Technical Program Expanded Abstracts*, 4854–4858.
- Thorbecke, J. W., C. P. A. Wapenaar, and G. Swinnen, 2004, Design of one-way wavefield extrapolation operators, using smooth functions in WLSQ optimization: *Geophysics*, **69**, 1037–1045.
- Vrolijk, J.-W., and G. Blacquiere, 2017, Shot-based deghosting for variable sea surface and

receiver depth: SEG Technical Program Expanded Abstracts 2017, 4887–4892.

FIGURE CAPTIONS

List of figure captions:

Figure 1 Model for the source ghost (a) and receiver ghost (b).

Figure 2 The Marmousi model used to create ghost-free synthetic data, with sources and receivers being positioned at a depth of 0 m. A water layer was 'added' to simulate a marine situation and boundaries were absorbing.

Figure 3 Ghost-free finite-difference data from the Marmousi model shown in Figure 2, a) typical ghost-free shot record, b) its frequency-wavenumber spectrum.

Figure 4 Marmousi data in the frequency-wavenumber domain, only a source ghost is present, a) shot record, b) receiver gather. Receivers at $z_d = 20$ m and sources at $z_s = 30$ m.

Figure 5 Marmousi data in the frequency-wavenumber domain, only a receiver ghost is present, a) shot record, b) receiver gather. Receivers at $z_d = 20$ m and sources at $z_s = 30$ m.

Figure 6 Marmousi data in the frequency-wavenumber domain, both a source ghost and a receiver ghost are present, a) shot record, b) receiver gather. Receivers at $z_d = 20$ m and sources at $z_s = 30$ m.

Figure 7 Data from a one-reflector medium in the frequency-wavenumber domain, both a source ghost and a receiver ghost are present, a) shot record, b) receiver gather. Receivers at $z_d = 20$ m and sources at $z_s = 30$ m.

Figure 8 Marmousi ZO data in the frequency-wavenumber domain, both a source ghost and a receiver ghost are present. Receivers at $z_d = 20$ m and sources at $z_s = 30$ m ($k_x = 0$)

m^{-1} component suppressed for better visibility).

Figure 9 Comparison of the frequency-wavenumber spectra of a receiver gather in a) and a ZO gather in b) of the Marmousi data for the case of a source ghost only ($z_s = 30$ m). The notches are deeper in the receiver gather than in the ZO data.

Figure 10 Frequency-wavenumber spectrum of Marmousi CMP data, both a source ghost and a receiver ghost are present. Receivers at $z_d = 20$ m and sources at $z_s = 30$ m.

Figure 11 Shot-record source deghosting; a) shot record with source ghost, b) shot record without source ghost, c) result of shot-record deghosting, d) error, i.e., difference between b) and c).

Figure 12 Receiver-gather source deghosting; a) receiver gather with source ghost, b) receiver gather without source ghost, c) result of receiver-gather deghosting, d) error, i.e., difference between b) and c).

Figure 13 Sea surfaces related to sea states 1 to 9.

Figure 14 Helmholtz-Kirchhoff integral geometry. The source (origin) is the red star, the observation point is the yellow triangle.

Figure 15 Marmousi model data in the frequency-wavenumber domain. Appearance of the notches for sea states 0 (top row), 6 (middle row) and 9 (bottom row) with $z_s = 30$ m and $z_d = 20$ m. Left: shot records, right: receiver gathers.

Figure 16 Source-ghost operators ($z_s = 30$ m) at three different lateral locations for a rough sea surface applied to the Marmousi data: sinusoidal sea surface (left), sea state 6 (right).

Figure 17 To compute the source ghost in the case of a dynamic rough sea surface, an

effective static rough surface is used. In a) the scheme for computing this effective surface is explained. It is composed of the parts that are hit by the source wavefield at subsequent time instances T_1, T_2, \dots, T_N . In 3-D, these parts have a circular shape, see some examples in b). The source depth is related to time instance T_1 .

Figure 19 Explanatory scheme for computing the dynamic rough sea effects on the receiver ghost. The result is obtained by extracting the relevant signal from a number of modeled shot records with receiver ghost, each with a different static rough sea surface, corresponding to subsequent moments in time.

Figure 18 Receiver gather with source ghost for the case of a dynamic sea surface with an average wave height of 10 m and $z_s = 20$ m in a) and its frequency-wavenumber spectrum in b). Each trace has been taken from a different shot record that has been modeled with its own effective dynamic sea surface. This explains the trace-to-trace jitter best observed in the zoomed inset in a).

Figure 20 The result of modeling the receiver ghost for the case of a static sea surface with mean wave height of 3.5 m is shown in a) and the corresponding frequency-wavenumber spectrum in d). This result should be compared with the one related to a dynamic sea surface as shown in b) and e). The differences are shown in c) and f) respectively.

Figure 21 The effective reflectivity is related to the part of the reflected wavefield that can be described by assuming a flat sea surface although in reality the sea surface is rough. In this example the effective reflectivity is allowed to be both frequency and angle dependent.

Figure 22 Example of using the effective reflectivity for deghosting. In a) the data with ghost are shown for a significant wave height of 3.5 m, in b) the deghosted result and in c) the residue. Here the effective reflectivity was frequency and angle dependent and the SNR

23.7 dB.

TABLE CAPTIONS

List of table captions:

Table 1 Description of sea states 0 to 9 and their correspondent significant wave height.

Table 2 SNR obtained using various approximations of $\bar{\mathbf{R}}$ for sea states 5 and 8.

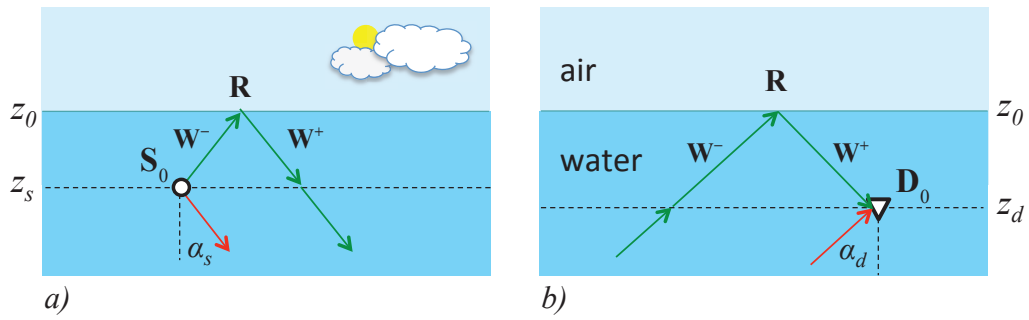


Figure 1: *Model for the source ghost (a) and receiver ghost (b).*

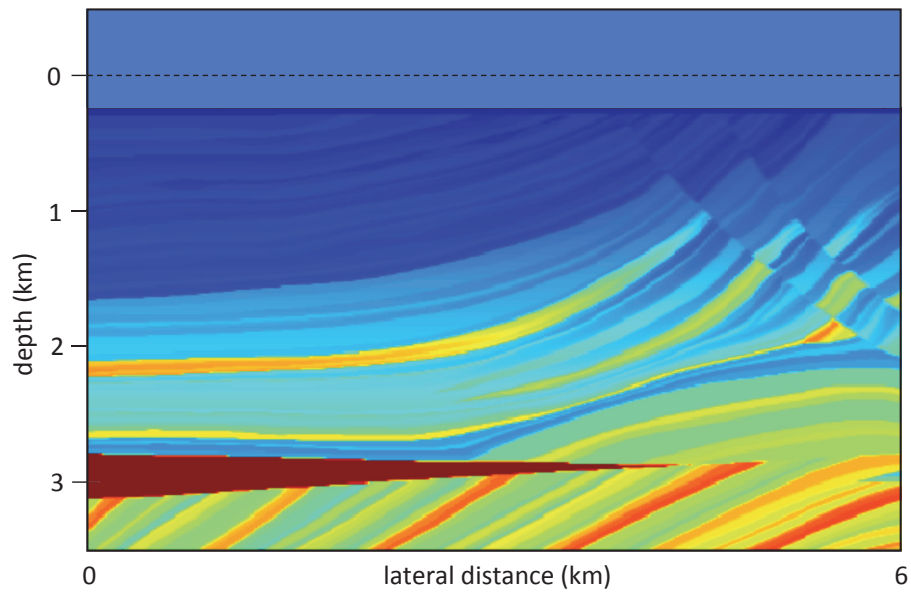


Figure 2: *The Marmousi model used to create ghost-free synthetic data, with sources and receivers being positioned at a depth of 0 m. A water layer was 'added' to simulate a marine situation and boundaries were absorbing.*

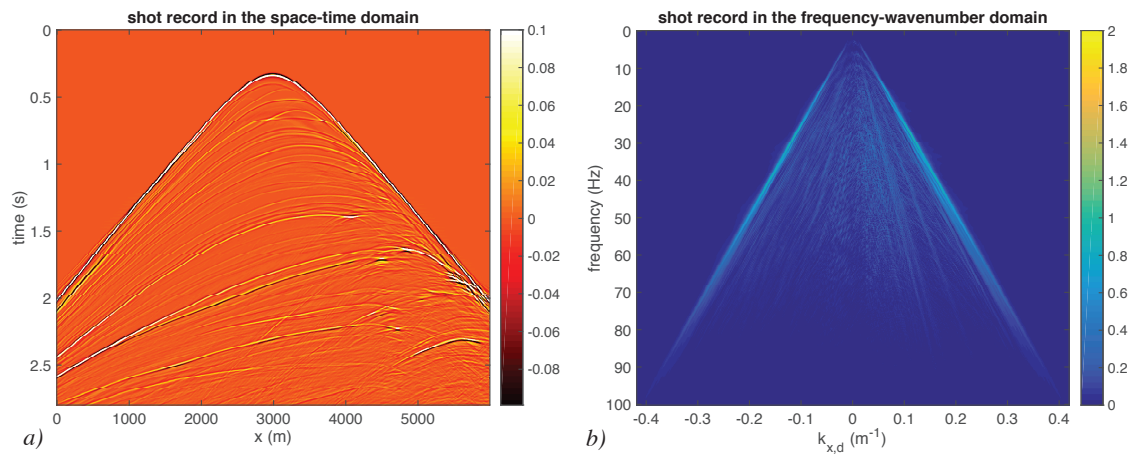


Figure 3: *Ghost-free finite-difference data from the Marmousi model shown in Figure 2, a) typical ghost-free shot record, b) its frequency-wavenumber spectrum.*

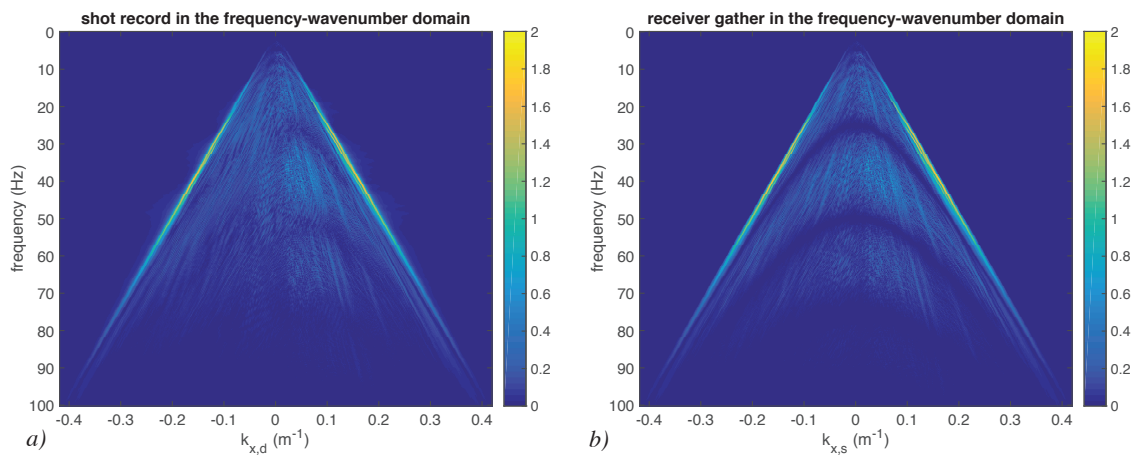


Figure 4: *Marmousi* data in the frequency-wavenumber domain, only a source ghost is present, a) shot record, b) receiver gather. Receivers at $z_d = 20$ m and sources at $z_s = 30$ m.

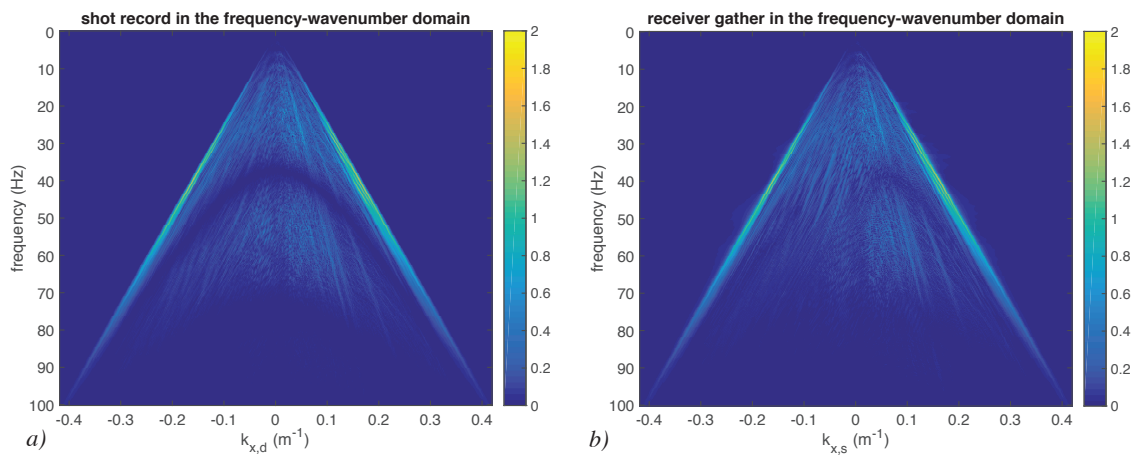


Figure 5: *Marmousi data in the frequency-wavenumber domain, only a receiver ghost is present, a) shot record, b) receiver gather. Receivers at $z_d = 20$ m and sources at $z_s = 30$ m.*

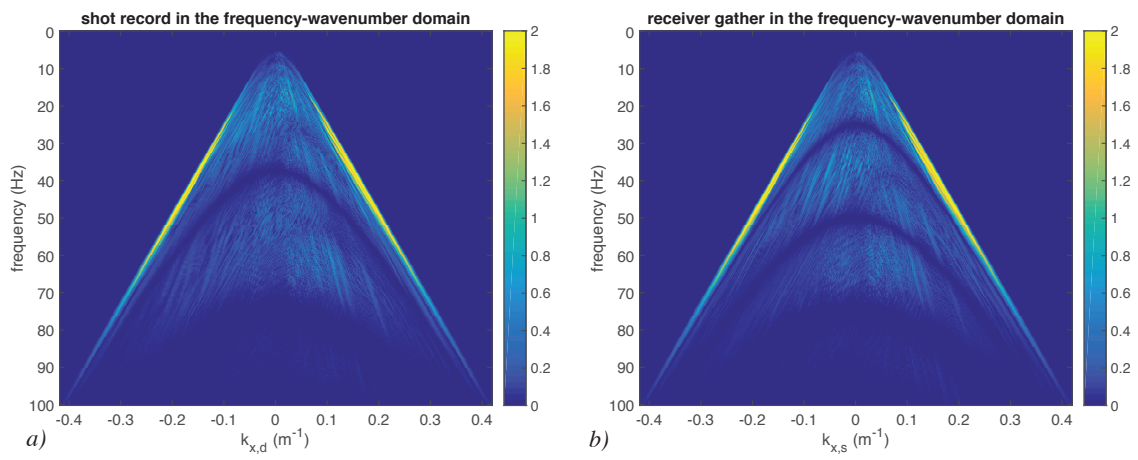


Figure 6: *Marmousi data in the frequency-wavenumber domain, both a source ghost and a receiver ghost are present, a) shot record, b) receiver gather. Receivers at $z_d = 20$ m and sources at $z_s = 30$ m.*

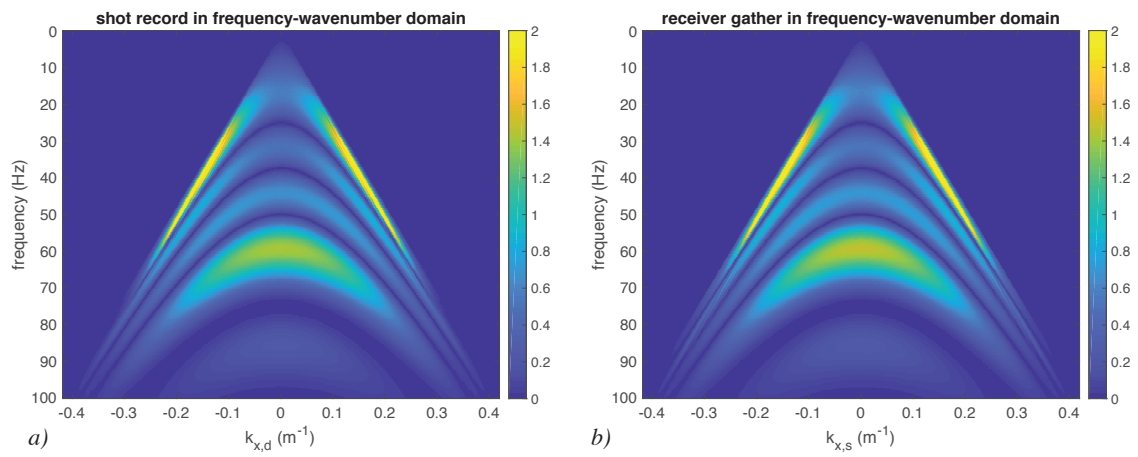


Figure 7: *Data from a one-reflector medium in the frequency-wavenumber domain, both a source ghost and a receiver ghost are present, a) shot record, b) receiver gather. Receivers at $z_d = 20$ m and sources at $z_s = 30$ m.*

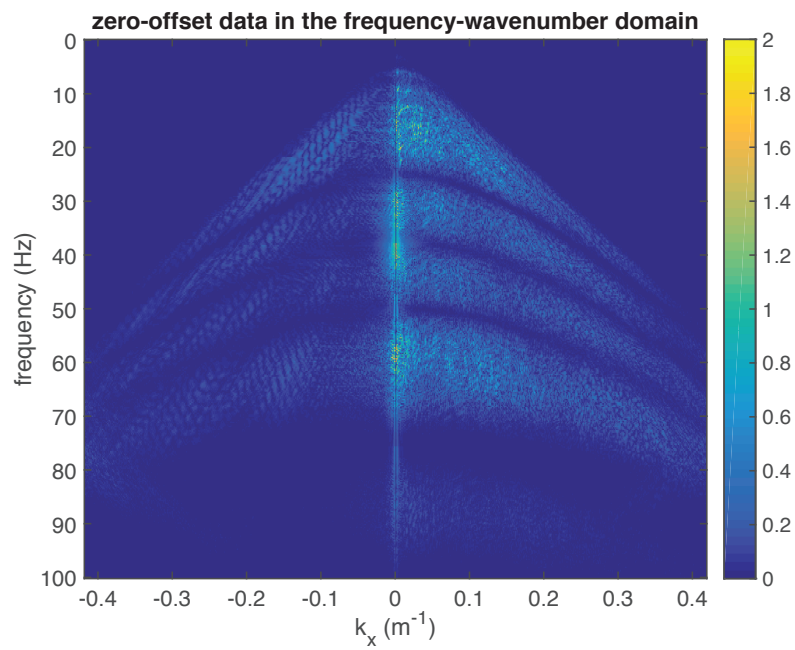


Figure 8: *Marmousi ZO data in the frequency-wavenumber domain, both a source ghost and a receiver ghost are present. Receivers at $z_d = 20$ m and sources at $z_s = 30$ m ($k_x = 0$ m⁻¹ component suppressed for better visibility).*

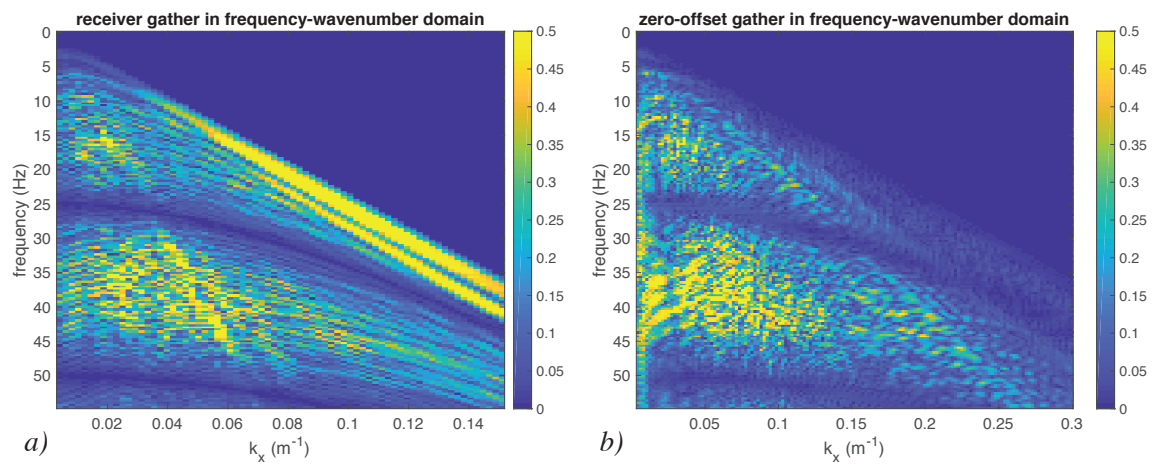


Figure 9: Comparison of the frequency-wavenumber spectra of a receiver gather in a) and a ZO gather in b) of the Marmousi data for the case of a source ghost only ($z_s = 30$ m). The notches are deeper in the receiver gather than in the ZO data.

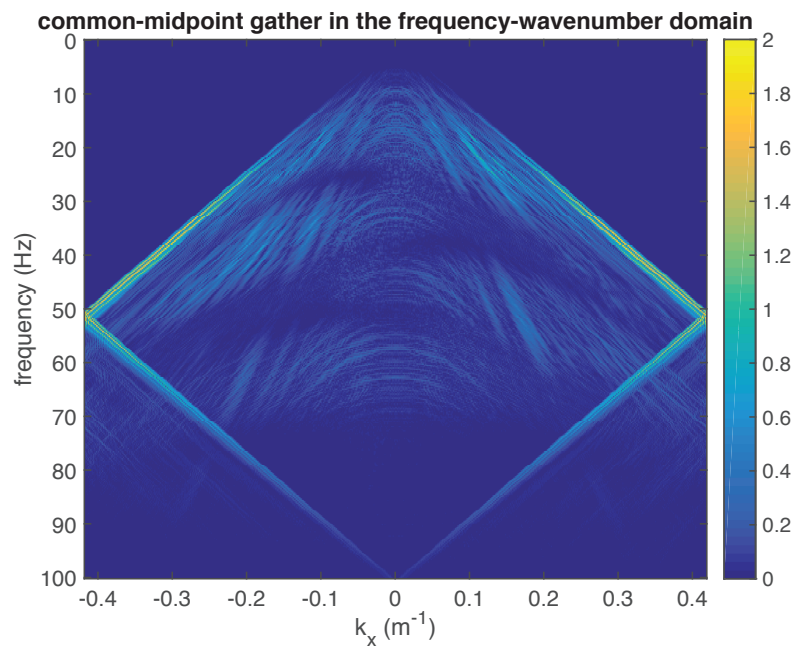


Figure 10: *Frequency-wavenumber spectrum of Marmousi CMP data, both a source ghost and a receiver ghost are present. Receivers at $z_d = 20$ m and sources at $z_s = 30$ m.*

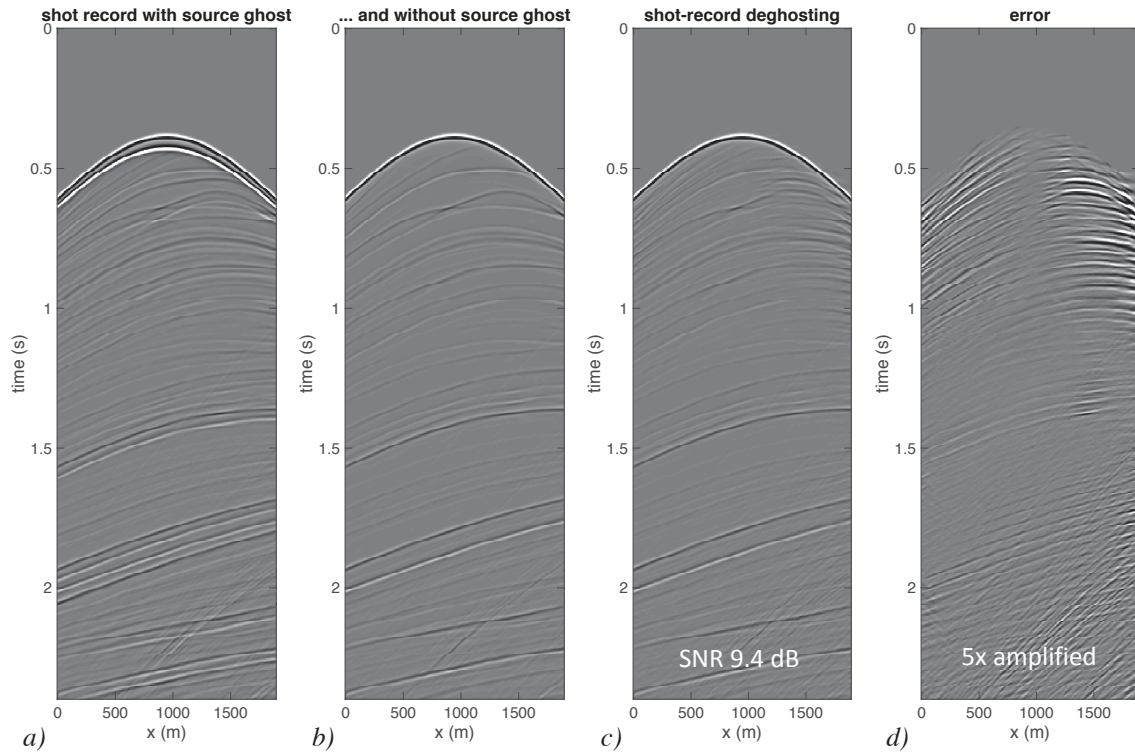


Figure 11: *Shot-record source deghosting; a) shot record with source ghost, b) shot record without source ghost, c) result of shot-record deghosting, d) error, i.e., difference between b) and c).*

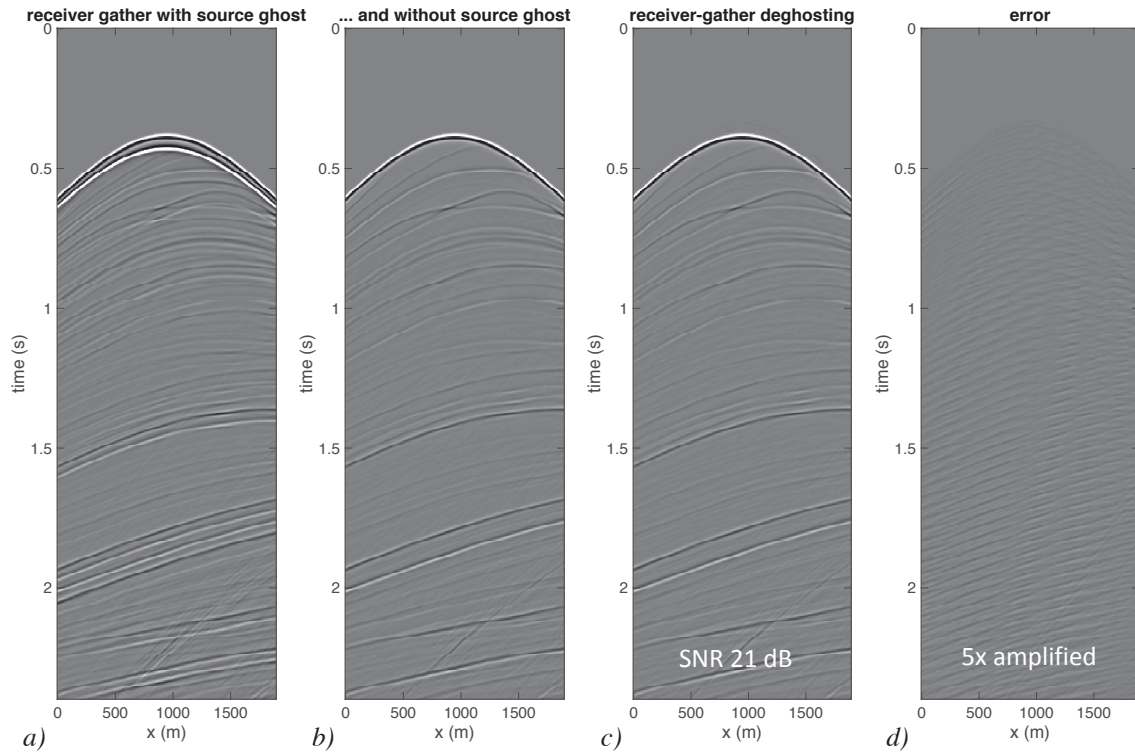


Figure 12: *Receiver-gather source deghosting; a) receiver gather with source ghost, b) receiver gather without source ghost, c) result of receiver-gather deghosting, d) error, i.e., difference between b) and c).*

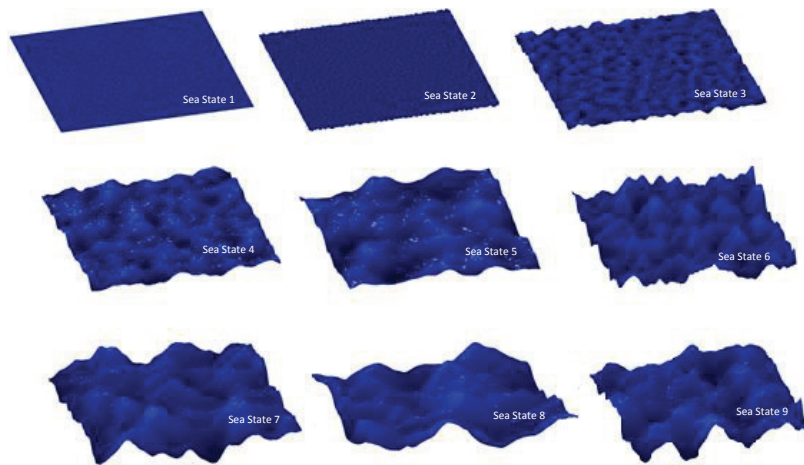


Figure 13: *Sea surfaces related to sea states 1 to 9.*

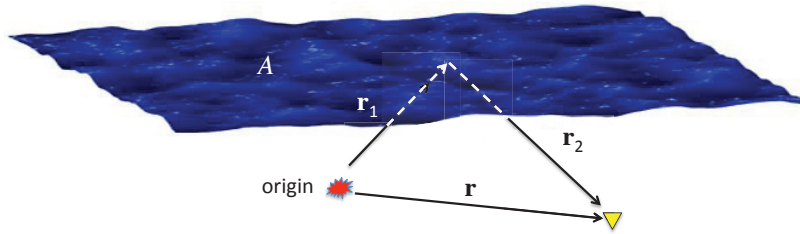


Figure 14: *Helmholtz-Kirchhoff integral geometry. The source (origin) is the red star, the observation point is the yellow triangle.*

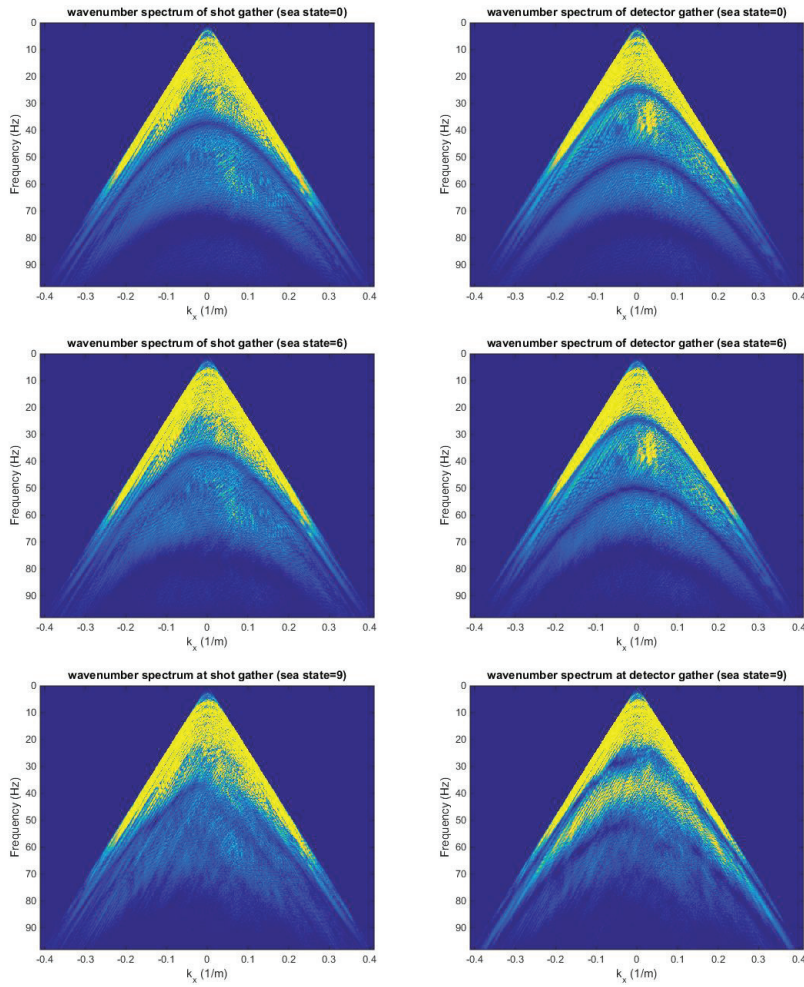


Figure 15: *Marmousi* model data in the frequency-wavenumber domain. Appearance of the notches for sea states 0 (top row), 6 (middle row) and 9 (bottom row) with $z_s = 30$ m and $z_d = 20$ m. Left: shot records, right: receiver gathers.

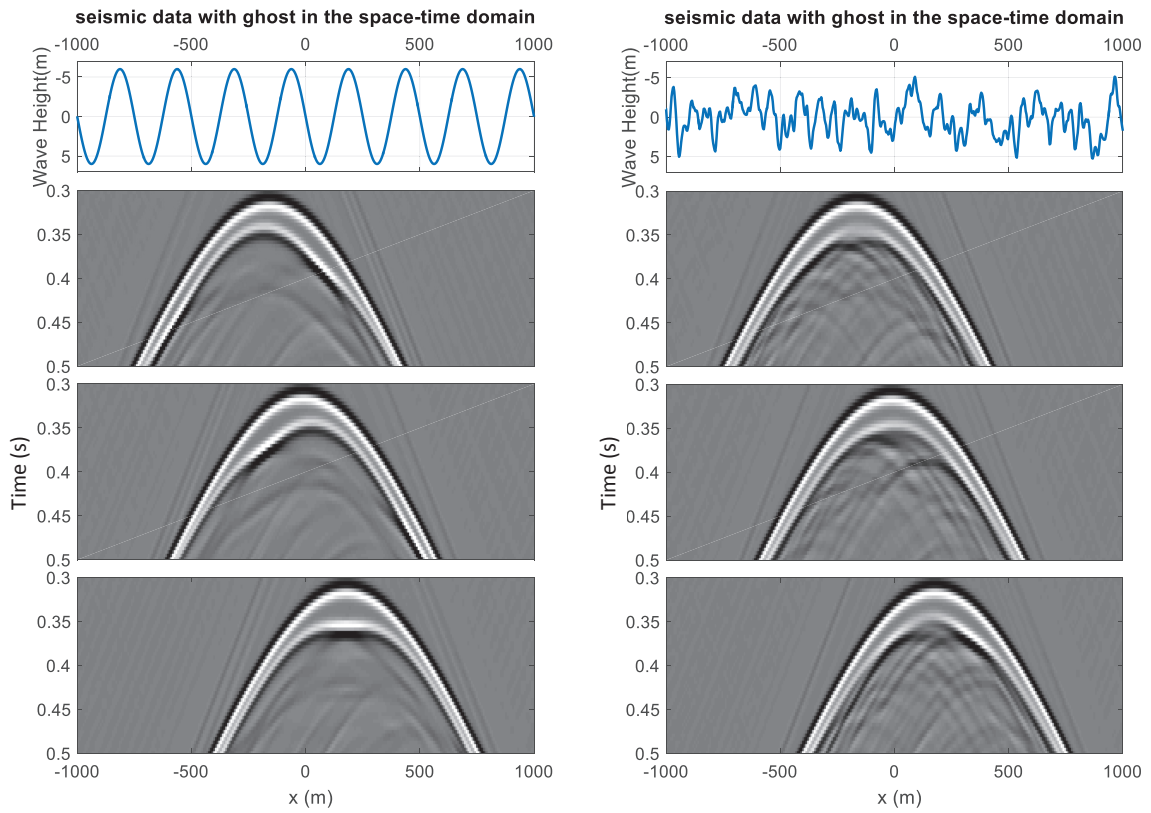


Figure 16: *Source-ghost operators ($z_s = 30$ m) at three different lateral locations for a rough sea surface applied to the Marmousi data: sinusoidal sea surface (left), sea state 6 (right).*

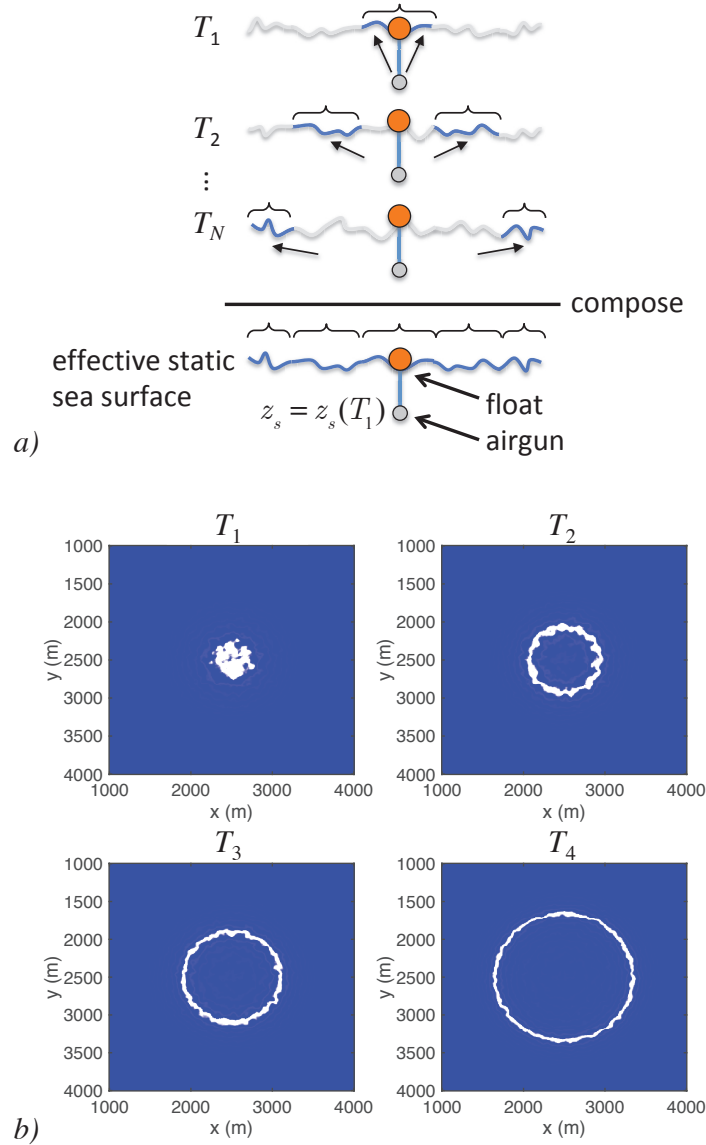


Figure 17: To compute the source ghost in the case of a dynamic rough sea surface, an effective static rough surface is used. In a) the scheme for computing this effective surface is explained. It is composed of the parts that are hit by the source wavefield at subsequent time instances T_1, T_2, \dots, T_N . In 3-D, these parts have a circular shape, see b). The source depth is related to time instance T_1 .

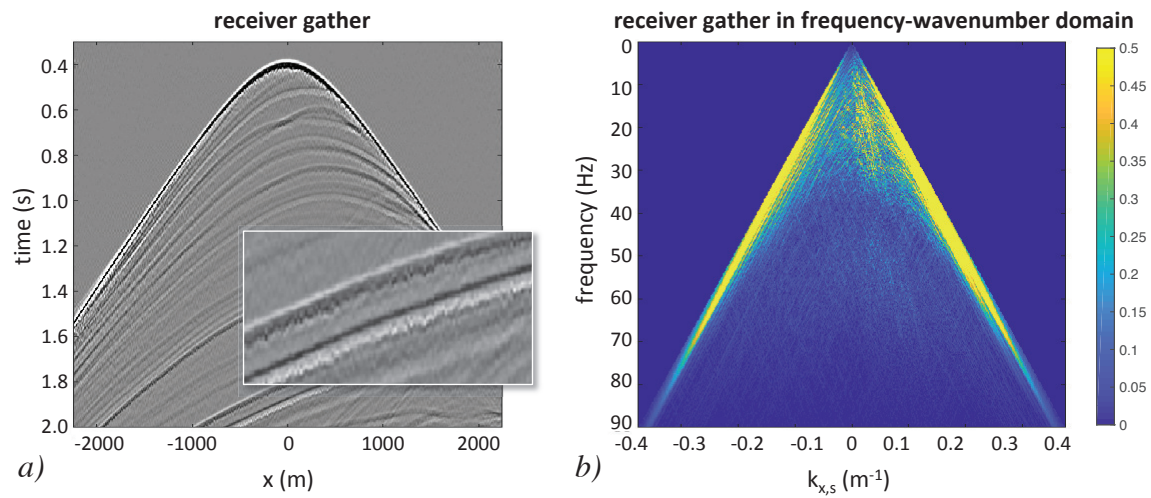


Figure 18: *Receiver gather with source ghost for the case of a dynamic sea surface with an average wave height of 10 m and $z_s = 20$ m in a) and its frequency-wavenumber spectrum in b). Each trace has been taken from a different shot record that has been modeled with its own effective dynamic sea surface. This explains the trace-to-trace jitter best observed in the zoomed inset in a).*

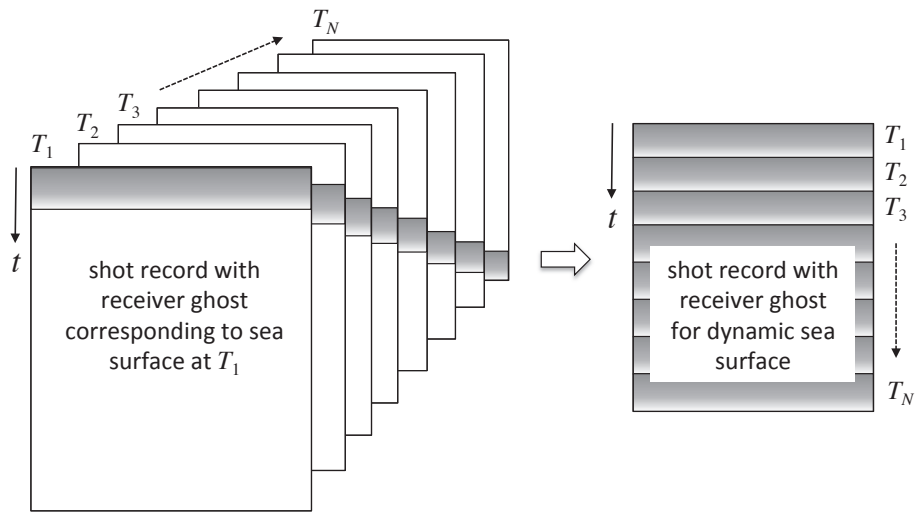


Figure 19: *Explanatory scheme for computing the dynamic rough sea effects on the receiver ghost. The result is obtained by extracting the relevant signal from a number of modeled shot records with receiver ghost, each with a different static rough sea surface, corresponding to subsequent moments in time.*

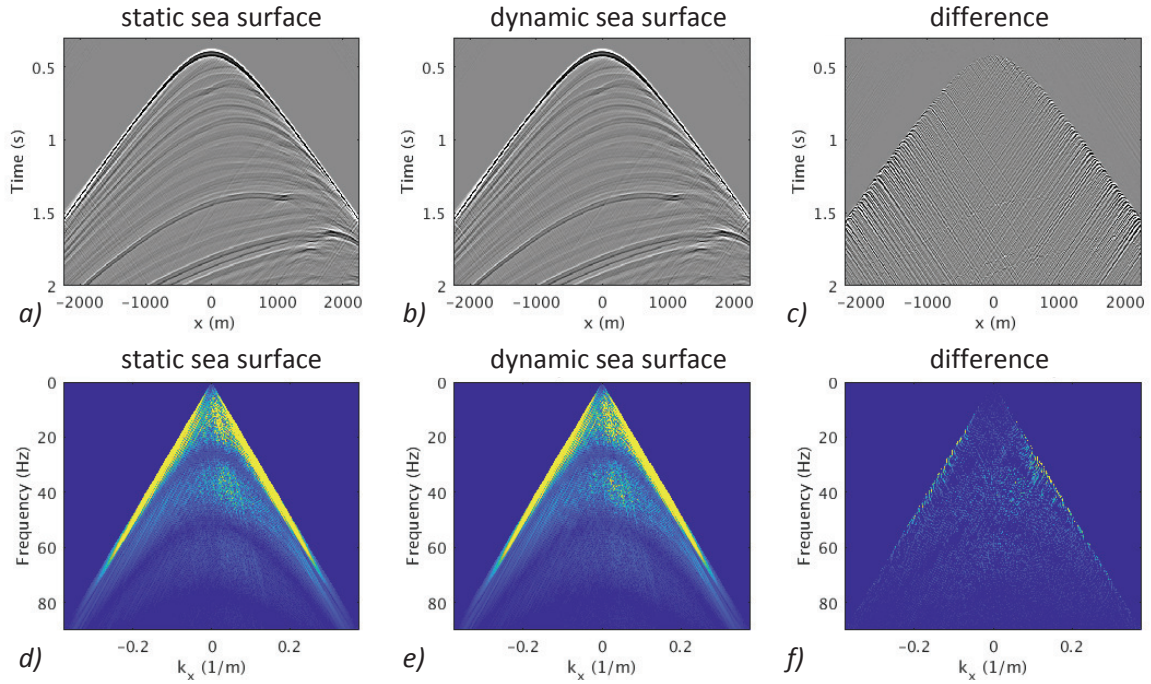


Figure 20: *The result of modeling the receiver ghost for the case of a static sea surface with mean wave height of 3.5 m is shown in a) and the corresponding frequency-wavenumber spectrum in d). This result should be compared with the one related to a dynamic sea surface as shown in b) and e). The differences are shown in c) and f) respectively.*

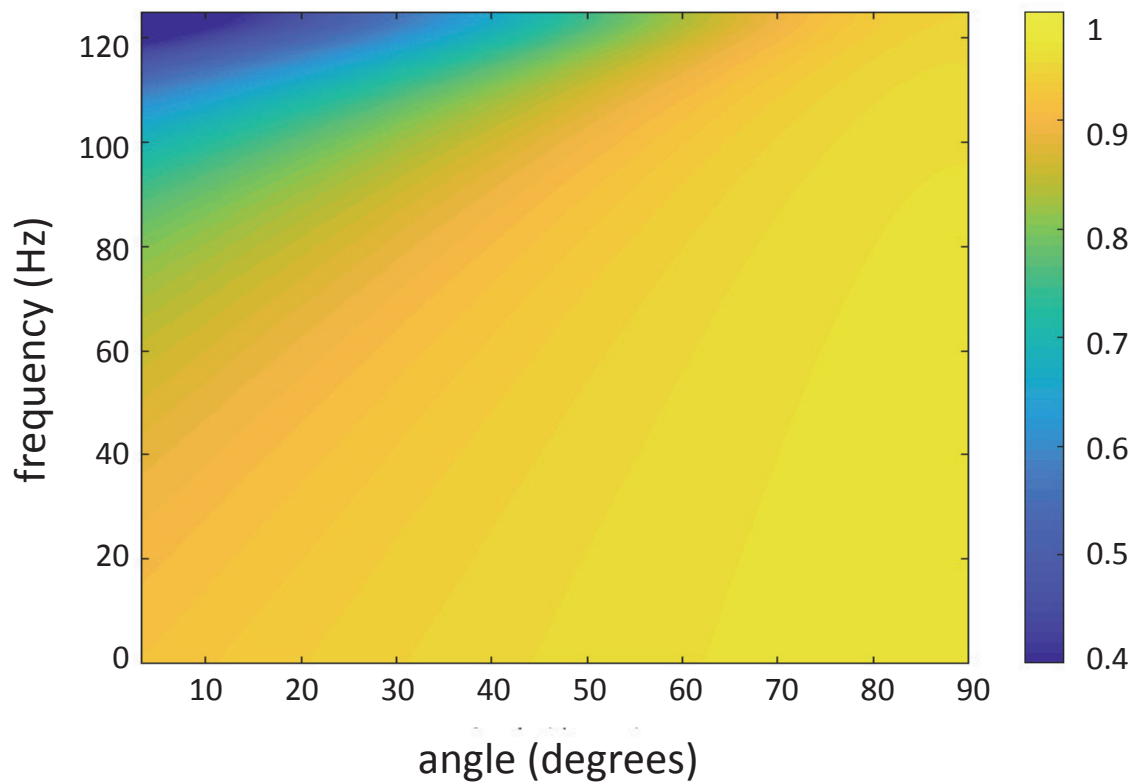


Figure 21: *The effective reflectivity is related to the part of the reflected wavefield that can be described by assuming a flat sea surface although in reality the sea surface is rough. In this example the effective reflectivity is allowed to be both frequency and angle dependent.*

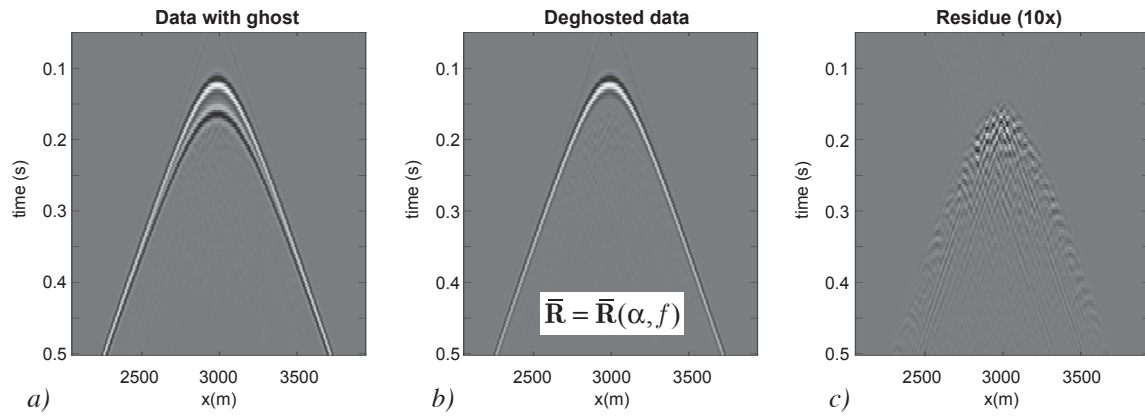


Figure 22: *Example of using the effective reflectivity for deghosting. In a) the data with ghost are shown for a significant wave height of 3.5 m, in b) the deghosted result and in c) the residue. Here the effective reflectivity was frequency and angle dependent and the SNR 23.7 dB.*

Sea state	Significant Wave Height (m)	Description
0	0	Calm (glassy)
1	0 - 0.1	Calm (rippled)
2	0.1 - 0.5	Smooth
3	0.5 - 1.25	Slight
4	1.25 - 2.5	Moderate
5	2.5 - 4	Rough
6	4 - 6	Very rough
7	6 - 9	High
8	9 - 14	Very high
9	> 14	Phenomenal

Table 1: *Description of sea states 0 to 9 and their correspondent significant wave height.*

Effective reflectivity	<i>SNR</i> (dB) SWH 3.5 m	<i>SNR</i> (dB) SWH 10 m
$\bar{\mathbf{R}} = -1$	23.5	10.0
$\bar{\mathbf{R}} = -0.99$	23.6	10.3
$\bar{\mathbf{R}}(f)$	23.6	10.5
$\bar{\mathbf{R}}(\alpha, f)$	23.7	10.7

Table 2: *SNR* obtained using various approximations of $\bar{\mathbf{R}}$ for sea states 5 and 8.